Journal Pre-proof

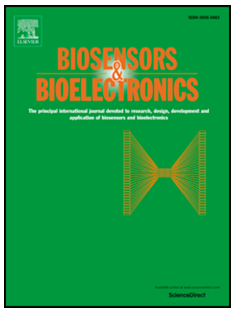

A synergistic promotion strategy remarkably accelerated electrochemiluminescence of SnO_2 QDs for MicroRNA detection using 3D DNA walker amplification

Fan Yang, Fang Yang, Ting-Ting Tu, Ni Liao, Ya-Qin Chai, Ruo Yuan, Ying Zhuo

PII: S0956-5663(20)30806-X

DOI: https://doi.org/10.1016/j.bios.2020.112820

Reference: BIOS 112820

To appear in: *Biosensors and Bioelectronics*

Received Date: 28 September 2020

Revised Date: 9 November 2020

Accepted Date: 11 November 2020

Please cite this article as: Yang, F., Yang, F., Tu, T.-T., Liao, N., Chai, Y.-Q., Yuan, R., Zhuo, Y., A synergistic promotion strategy remarkably accelerated electrochemiluminescence of SnO_2 QDs for MicroRNA detection using 3D DNA walker amplification, *Biosensors and Bioelectronics* (2020), doi: https://doi.org/10.1016/j.bios.2020.112820.

Credit Author Statement

Fan Yang: Conceptualization, Methodology, Investigation, Data curation, Writing - original draft, Writing - review & editing.

Fang Yang: Conceptualization, Data curation.

Ting-Ting Tu: Data curation, Formal analysis.

Ni Liao: Software, Data curation.

Ya-Qin Chai: Resources, Supervision.

Ruo Yuan: Funding acquisition, Resources, Project administration, Supervision.

Ying Zhuo: Funding acquisition, Resources, Writing - review & editing, Supervision.

A Synergistic Promotion Strategy Remarkably Accelerated Electrochemiluminescence of SnO_2 QDs for MicroRNA Detection using 3D DNA Walker Amplification

Fan Yang[a], Fang Yang[a], Ting-Ting Tu[a], Ni Liao[a, b], Ya-Qin Chai[a], Ruo Yuan[a] and Ying Zhuo[a,*]

[*] Corresponding authors at: **Tel**.: +86 23 68253172, **fax**: +86 23 68253172.

E-mail addresses: yingzhuo@swu.edu.cn (Y. Zhuo)

a Key Laboratory of Luminescence Analysis and Molecular Sensing (Southwest University), Ministry of Education, College of Chemistry and Chemical Engineering, Southwest University, Chongqing 400715, PR China

b College of Biological and Chemical Engineering, Panzhihua University, Panzhihua 617000, PR China

ABSTRACT:

Developing low-cost and efficient methods to enhance the electrochemiluminescence (ECL) intensity of luminophores is highly desirable and challenging. Herein, we develop a synergistic promotion strategy based on three types of co-reaction accelerators to achieve an efficient SnO_2 quantum dots (SnO_2 QDs)-based ternary ECL system. Specifically, the MnO_2 nanoflowers (MnO_2 NFs), Ag nanoparticles (Ag NPs) and hemin/G-quadruplex were rationally selected as co-reaction accelerators. Owing to the synergistic effect, the deft integration of three types of co-reaction accelerators enabled better structural stability, more exposed catalytic active sites, and faster charge transfer, thus more effectively facilitating the reduction of co-reactant ($S_2O_8^{2-}$) compared with that of the single co-reaction accelerator. To demonstrate the practical utility of this principle, an "on-off-super on" ECL biosensor was constructed in combination with a 3D DNA walker, which showed a superior linear range (10 aM to 100 pM) and a low detection limit (2.9 aM) for the highly-sensitive miRNA-21 detection. In general, this work firstly reported that three types of co-reaction accelerators were deftly integrated to remarkably amplify the ECL emission of SnO_2 QDs, and provided brand-new perspectives for research on the ingenious design of the structure and component of highly efficient co-reaction accelerators.

Keywords: ECL; SnO_2 quantum dots; MnO_2 nanoflowers; Ag nanoparticles; hemin/G-quadruplex; synergistic promotion strategy

1. Introduction

Since the electrochemiluminescence (ECL) phenomenon of silicon nanocrystal quantum dots was firstly investigated and reported by Bard's group in 2002, quantum dots (QDs) have attracted keen concern owing to their unique features of quantum size effect, excellent photostability and long fluorescence lifetime (Bruchez et al., 1998; Ding et al., 2002). Despite, the wide applications of different highly luminescent QDs in biosensing fields, such as CdTe QDs, CdSe QDs and PbS QDs, the high toxicity and low abundance of elements restricted their biological applications fundamentally (Shi et al., 2017; Dai et al., 2017; Yang et al., 2018). Therefore, it is a challenging and interesting subject to explore other high-luminescent quantum dots with low toxicity and accessibility (Dong et al., 2017). The SnO_2 QDs have become a hot topic for researchers due to the low cost, environmental friendliness and excellent photoelectronic properties (Zhang et al., 2019; Wang et al., 2018). However, the high enough energy is required to achieve the transition of valence electrons from the valence band to the conduction band due to the wide band gap (E_g = 3.6 eV at 300 K), thus the low yield of free electrons or holes results in the low luminescent intensity of SnO_2 QDs (Xu et al., 2008). In 2015, our group first proposed an effective avenue to improve the ECL intensity by the co-reaction accelerator, which could promote the reaction efficiency between luminophores and co-reactants (Ma et al., 2015). Inspired by this, finding high-efficiency co-reaction accelerators of SnO_2 QDs is a practical approach to enhance their ECL intensity.

As a classical co-reactant, peroxydisulfate ($S_2O_8^{2-}$) is commonly employed to enhance the cathodic ECL signal of various kinds of luminophores due to the

electrochemical interaction between the intermediates of co-reactant and luminophores. Recently, a number of co-reaction accelerators have been reported to promote the reduction of $S_2O_8^{2-}$ for more oxidizing intermediate ($SO_4^{\bullet-}$) production, such as Fe_3O_4 nanoparticles (Keyikoglu et al., 2020), graphene nanosheets (Zhu et al., 2020), metal organic framework (MOF) (Zhou et al., 2020a), and semicarbazide (Sem) (Ma et al., 2015), etc. However, a single type of co-reaction accelerator was usually applied in these ternary ECL systems. Based on the synergistic effect of multi-components, the combination of multiple co-reaction accelerators is considered to be a desirable approach, which significantly improved the reaction efficiency between luminophores and co-reactants to generate a large amount of the active intermediates of co-reactant (Zhou et al., 2020b). Herein, a synergistic promotion strategy based on three types of co-reaction accelerators was presented, where the MnO_2 nanoflowers (MnO_2 NFs), Ag nanoparticles (Ag NPs) and hemin/G-quadruplex were rationally selected as co-reaction accelerators. Specifically, the MnO_2 NFs served as an effective matrix to enable structural stability and provide high surface areas to contribute the full exposure of catalytic active sites based on its unique porous structure and excellent electrocatalytic activity (Reddy et al., 2009; Chen et al., 2010; Xue et al., 2016). Secondly, the Ag NPs not only improved conductivity and increased catalytic active sites to facilitate charge transfer due to its superior electrical conductivity (Shifrina et al., 2020; Khan et al., 2020), but also supplied abundant binding sites to cross-link with capture probes (CPs). Third, well-known as a kind of co-reaction accelerator, the hemin/G-quadruplex structures could combine with DNA

amplification strategies ingeniously (Li et al., 2020a). Benefiting from the rational material selection, rigorous structural design and synergistic effect, the deft integration of three types of co-reaction accelerators could more effectively promote the reduction of $S_2O_8^{2-}$ in comparison with the single co-reaction accelerator, thus remarkably amplifying the ECL emission of SnO_2 QDs.

Here-after, we combined a synergistic promotion strategy based on three types of co-reaction accelerators and 3D DNA walker machine to propose an "on-off-super on" ECL biosensor for miRNA-21. Initially, as presented in Scheme 1A, the multifunctional nanocomposites of accelerator-luminophore-accelerator were dropped on the surface of the bare glassy carbon electrode (GCE) to attain an obvious ECL initial signal with $S_2O_8^{2-}$ as co-reactant ("on" state). Specifically, MnO_2 NFs, Ag NPs were used as co-reaction accelerators and SnO_2 QDs was luminophore. Then, capture probes (CPs) with G-rich sequence, double-labeled ferrocene quencher probes (Fc-DNA-Fc) were modified on the electrode successively to form triplex DNA structures. Compared with the common single-labeled ferrocene quencher probes (DNA-Fc), the quenching effect of Fc-DNA-Fc was much better, thus achieving an extraordinarily low background signal ("off" state) (Kitamura et al., 2020). Subsequently, the target miRNA-21 was converted to mimic targets (MT) based on 3D DNA walker amplification where one target miRNA-21 binding could trigger a few times of Zn^{2+} cleavage action, resulting in a large number of MT production (Scheme 1B) (Wang et al., 2019; Li et al., 2020b). Finally, after incubating with MT to make the Fc-DNA-Fc removed from the electrode surface, hemin was dropped on

the resultant electrode to form massive hemin/G-quadruplex structures which acted as the third kind of co-reaction accelerator, reaching an extraordinarily strong ECL signal ("super on" state). Overall, this work provides a synergistic promotion strategy based on three types of co-reaction accelerators, which led to better structural stability and more significant promotion on the reduction of $S_2O_8^{2-}$, thus effectively enhancing the ECL intensity of SnO_2 QDs to achieve the ultrasensitive detection of miRNA-21.

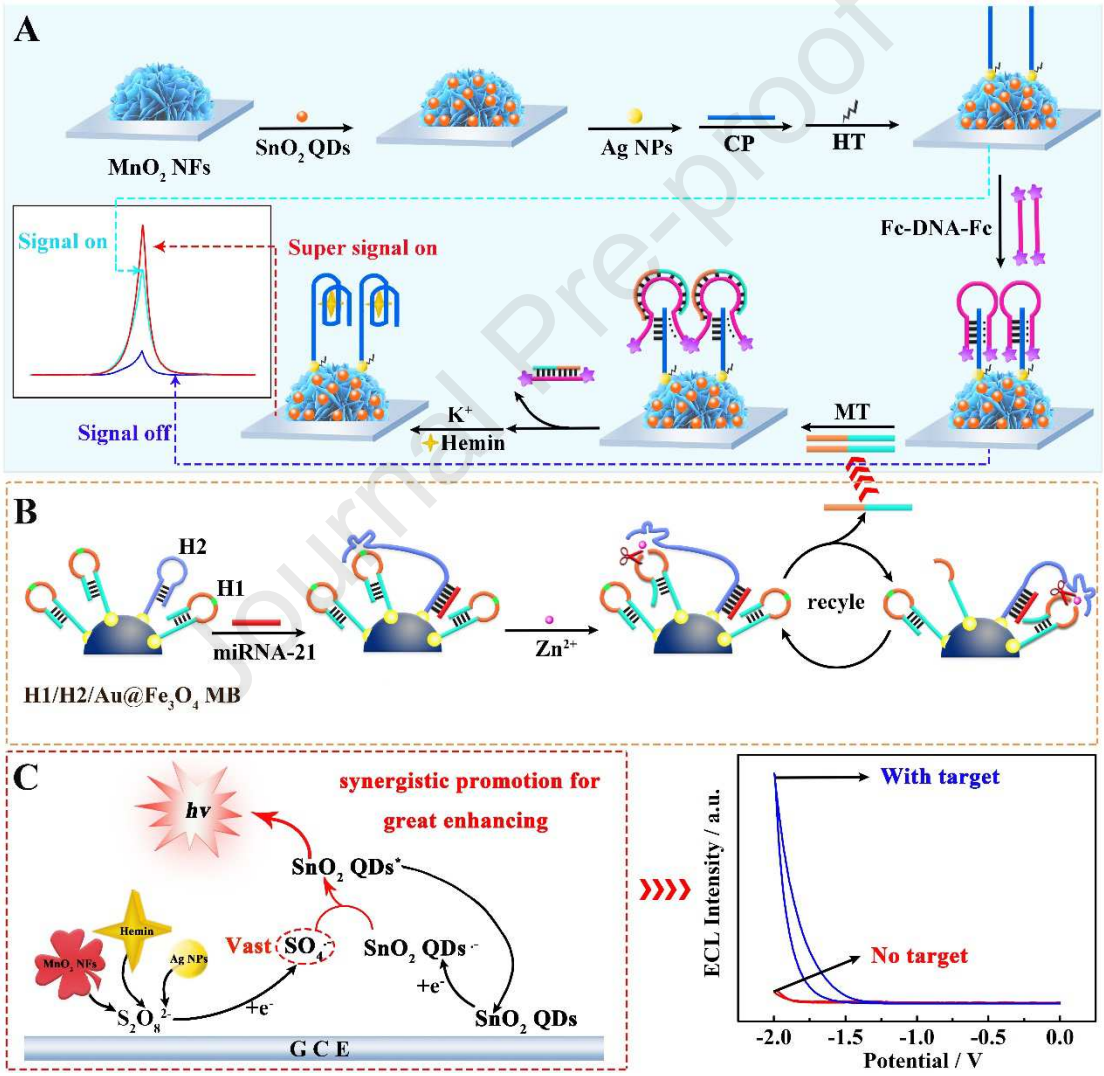

Scheme 1. Schematic illustration of the proposed ECL biosensor for miRNA-21 detection: (A) The fabrication of the Ag NPs/SnO_2 QDs/MnO_2 NFs based-ECL biosensor. (B) The process of the 3D DNA walker amplification. (C) The ECL enhancement mechanism of synergistic promotion strategy.

2. Experimental section

2.1. Preparation of SnO_2 QDs and MnO_2 NFs

The synthesis of SnO_2 QDs was illustrated in Section 3 of the Supporting Information. The MnO_2 NFs were synthesized referring to a previously literature report (Lu et al., 2016). First, 0.05 mmol $KMnO_4$ was dissolved in 2 mL deionized water. Then 14 mL glucose solution (0.01 M) was added dropwise to the abovementioned solution under vigorous stirring, followed by an intense stirring of the mixture for 0.5 h. After centrifugation and 3 times of deionized water washing, the final precipitates were obtained. At last, the MnO_2 NFs were redispersed in 5 mL of deionized water for later use.

2.2. Assembly of the ECL biosensor

Before using, the bare GCE was polished and sonicated using the previous method (Ma et al., 2015). Next, 5 μL of the MnO_2 NFs solution were added dropwise to the cleaned bare GCE surface and dried at 37 °C. Afterwards, 3 μL of the SnO_2 QDs solution and 2 μL of the Ag NPs solution (as-prepared in Section 4 of the Supporting Information) were coated onto the resultant electrode and dried at 37 °C successively. Through the above steps, the multifunctional layer of Ag NPs/SnO_2 QDs/MnO_2 NFs was formed via electrostatic interaction (the zeta potential values of MnO_2 NFs, SnO_2 QDs and Ag NPs are shown in Section 6 of the Supporting Information). After that, 5 μL of capture probes (CPs, 2 μM) with amino group were incubated on Ag NPs/SnO_2 QDs/MnO_2 NFs/GCE and placed at 4 °C overnight. In this process, the CPs were immobilized on the surface of modified electrode via Ag-N bond. Subsequently, 10 μL of 1 mM hexanethiol (HT) were dropped on the resultant

electrode surface and kept for 1 h, thus restraining nonspecific binding. Finally, the HT/CPs/Ag NPs/SnO_2 QDs/MnO_2 NFs/GCE was incubated with 5 μL of 2 μM double-labeled ferrocene quencher probes (Fc-DNA-Fc) at 37 °C for 2 h, forming plenty of triplex DNA structures for subsequent experiments. After each procedure, the fabricated electrode was washed using deionized water thoroughly to make the unbound residue removed.

2.3. Process of the 3D DNA walker amplification

First, 20 μL of hairpin 1 (H1, 2 μM, used as substrate probes) and 2 μL of hairpin 2 (H2, 2 μM, used as walker probes) were added into 40 μL of Fe_3O_4@Au NPs (as-prepared in Section 5 of the Supporting Information), and then gently shaken at 4 °C overnight and magnetically separated to produce the 3D DNA walker machine. Then, the mixture which included 2 μL of target miRNA-21 (with various concentrations), 8 μL $ZnCl_2$ (5 μM) solution and 10 μL of 3D DNA walker machine solution were incubated at 37 °C for 70 min. In this process, H2 opened its hairpin structure due to partial hybridization with target miRNA-21, which made the unhybridized part of the opened H2 to bind with H1 and generate the recognition site for Zn^{2+}. In presence of Zn^{2+}, H2 walked around the wide 3D track to realize the high-efficiency cleavage of H1 for extensive single-strand fragments production which were operated as mimic targets (MT). Hence, a large number of MT were obtained after magnetic separation, which was used for the subsequent experimental procedure.

2.4. Measurement procedure

Initially, the prepared ECL biosensor was incubated with 5 μL of MT solution at 37 °C for 2 h. In this process, Fc-DNA-Fc removed from the electrode surface due to its hybridization with MT. After cleaned with deionized water to remove the residue, the resultant electrode was incubated with 5 μL hemin (0.2 mM) in 10 mM 4-(2-hydroxyethyl) piperazine-ethanesulfonic acid sodium salt (HEPES) buffer (pH 7.0, 40 mM KCl, 1% dimethyl sulfoxide) at room temperature for 1 h to generate massive hemin/G-quadruplex structures. Finally, the obtained biosensor was immersed into 2 mL PBS solution (pH 7.4) containing 10 mM $S_2O_8^{2-}$ to detect the ECL signal using a MPI-A ECL analyzer. Additionally, the working potential varied from -2 to 0 V and the photomultiplier tube (PMT) voltage was set as 800 V.

3. Results and discussion

3.1. Characterization of the MnO_2 NFs and SnO_2 QDs nanomaterials

Scanning electron microscopy (SEM) image of MnO_2 NFs presented a flower-like structure with a diameter of about 100 nm (Figure 1A), which was coherent with previous work (Lu et al., 2016). The high-resolution transmission electron microscopy (HRTEM) revealed that the lattice spacing of SnO_2 QDs were 0.33 nm and 0.26 nm (Figure 1B), which matched with the (110) and (111) lattice plane of tetragonal SnO_2 respectively (Dutta et al., 2014). And it also showed that the size of the prepared SnO_2 QDs was 2-4 nm. The selected area electron diffraction (SAED) pattern of SnO_2 QDs displayed a few diffraction rings (Figure 1C), which were well consistent with the tetragonal structure of SnO_2 QDs (ICDD file no. 41-1445), indicating the SnO_2 QDs were well crystallized. Furthermore, X-ray photoelectron spectroscopy (XPS) of SnO_2 QDs was applied for elemental analysis. Typically, the four characteristic peaks including Sn 4d, Sn 3d, Sn 3p and O 1s were observed clearly in Figure 1D. Besides, as displayed in Figure 1E, two characteristic peaks of Sn 3d were located at 485.7 and 496.2 eV, corresponding to Sn $3d_{5/2}$ and Sn $3d_{3/2}$, respectively (Chu et al., 2019). The peak at 531.9 eV in Figure1F was assigned to O 1s (Gao et al., 2020). It was obvious that SnO_2 QDs had been successfully synthesized according to the above characterization results.

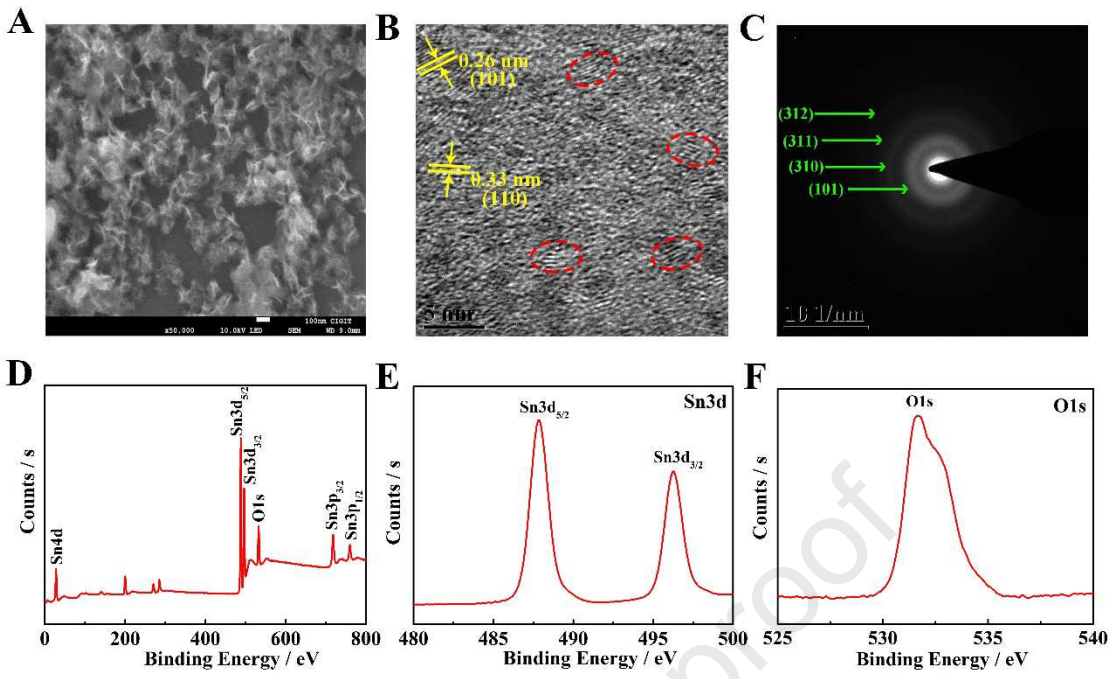

Fig. 1. (A) SEM characterization of the MnO_2 NFs. (B) HR-TEM image (scale bar, 5 nm) and (C) SAED pattern of the SnO_2 QDs. XPS analysis of the full region of SnO_2 QDs (D), Sn 3d region (E), and O 1s region (F).

3.2. PL and ECL spectra of the SnO_2 QDs

The ECL, photoluminescence (PL) spectra were applied to investigate the optical properties of SnO_2 QDs. First, the ECL spectra of SnO_2 QDs/$S_2O_8^{2-}$ system was characterized by 3D color map surface (Figure 2A) and heat map image (Figure 2B), indicating that the maximum ECL emission was 650 nm. Furthermore, from the PL spectra of SnO_2 QDs (curve *a* in Figure 2C), the strongest PL emission peak was at 403 nm when the excitation wavelength was set at 357 nm (Xu et al., 2008). Distinctly, the maximum ECL emission peak (curve *b* in Figure 2C) showed an evident red-shift of 247 nm in contrast with the PL spectra, which was also observed in other nanocrystal quantum dots (Ding et al., 2002; Zheng et al., 2009; Myung et al., 2002; Lei et al., 2020). This was because ECL mainly originated from the surface states, while PL mainly occurred through excitation and emission within the nanocrystal core.

Quantitatively, the energy separation of surface states was lower than the band gaps of nanocrystal core (Zheng et al., 2009; Myung et al., 2002).

Subsequently, the ECL spectra of the GCE under four different conditions were investigated. As exhibited in Figure 2D, the maximum ECL emission peak of MnO_2 NFs/GCE in $S_2O_8^{2-}$ solution was 680 nm (curve *b* in Figure 2D), which was in accordance with that of the bare GCE in $S_2O_8^{2-}$ solution (curve *a* in Figure 2D), giving evidence that the luminophore in both systems was the $^1(O_2)_2^*$ in $S_2O_8^{2-}$ solution (Khan et al., 1970). While the maximum ECL emission peak of SnO_2 QDs/GCE in $S_2O_8^{2-}$ solution located at 650 nm (curve *c* in Figure 2D), implying that the luminophore was SnO_2 QDs^* in $S_2O_8^{2-}$ solution (Lei et al., 2020). As expected, when the SnO_2 QDs/MnO_2 NFs/GCE was tested in $S_2O_8^{2-}$ solution, the maximum ECL emission peak located at 650 nm as well (curve *d* in Figure 2D), declaring that the luminophore of this SnO_2 QDs/$S_2O_8^{2-}$/MnO_2 NFs system was also SnO_2 QDs^*. More importantly, the ECL intensity (curve *d* in Figure 2D) was about 1.5 times higher than that of SnO_2 QDs/GCE in $S_2O_8^{2-}$ solution (curve *c* in Figure 2D), confirming that MnO_2 NFs served as a co-reaction accelerator to improve the ECL signal of SnO_2 QDs in $S_2O_8^{2-}$ system.

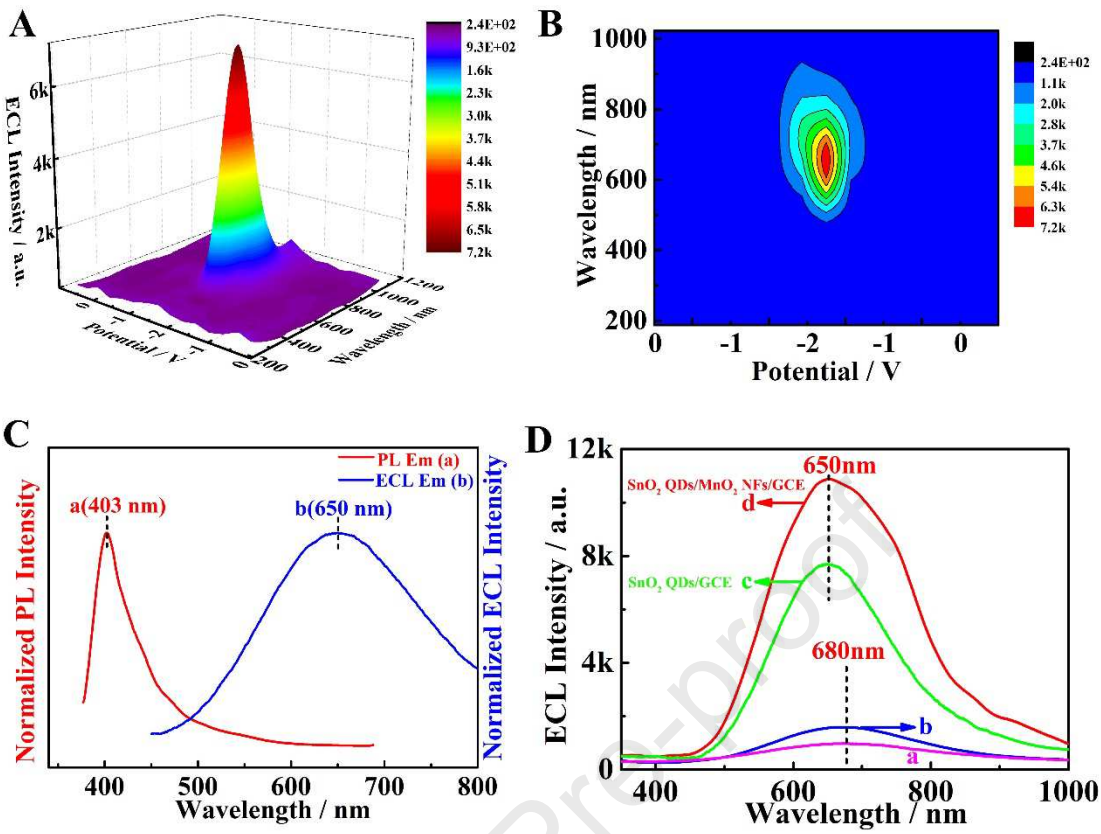

Fig. 2. The 3D ECL spectra of SnO_2 QDs in $S_2O_8^{2-}$ solution: (A) color map surface, (B) heat map image. (C) PL emission spectra by setting the excitation wavelength at 357 nm (a) and ECL emission spectra (b) of SnO_2 QDs. (D) ECL spectra of the bare GCE (a), MnO_2 NFs/GCE (b), SnO_2 QDs/GCE (c) and SnO_2 QDs/MnO_2 NFs/GCE (d) in $S_2O_8^{2-}$ solution. The concentration of $S_2O_8^{2-}$ was 25 mM in 0.1 M PBS (pH 7.4).

3.3. ECL enhancement mechanism of the Ag NPs/SnO_2 QDs/MnO_2 NFs nanocomposite

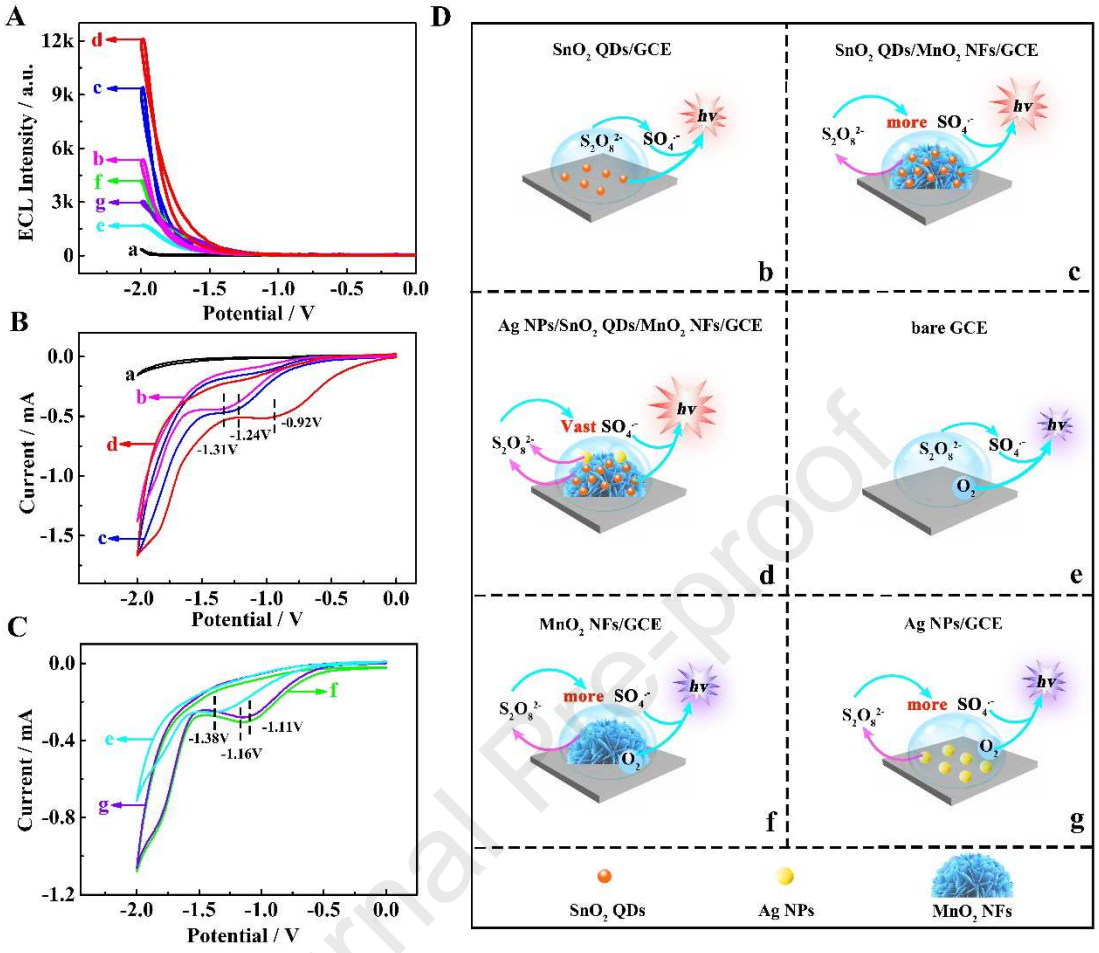

Fig. 3. (A) ECL-potential profiles and (B, C) CVs of the different modified electrodes: the SnO_2 QDs/GCE in PBS solution (a), SnO_2 QDs/GCE (b), SnO_2 QDs/MnO_2 NFs/GCE (c), Ag NPs/SnO_2 QDs/MnO_2 NFs/GCE (d), bare GCE (e), MnO_2 NFs/GCE (f) and Ag NPs/GCE (g) in $S_2O_8^{2-}$ solution. The concentration of $S_2O_8^{2-}$ was 10 mM in 0.1 M PBS (pH 7.4). (D) Schematic illustration for possible luminescence mechanism of different modified electrodes.

To illustrate the possible ECL enhancement mechanism, we measured the ECL and cyclic voltammetry (CV) curves of different modified electrodes synchronously under the working potential ranging from -2 to 0 V. The ECL signal of the SnO_2 QDs/GCE in PBS solution was as weak as 325 a.u. (curve *a* in Figure 3A), which was produced by the excited state of SnO_2 QDs (SnO_2^*). With the aid of $S_2O_8^{2-}$, the ECL intensity observably increased from 325 a.u. to 5356 a.u. (curve *b* in Figure 3A) due to $S_2O_8^{2-}$ acting as a co-reactant. Additionally, compared with curve *a* in Figure 3B

without distinct redox peaks, the corresponding CV curve showed a noticeable reduction peak at -1.31 V (curve *b* in Figure 3B), which was attributed to the reduction of $S_2O_8^{2-}$ (Fabrizio et al., 2000). Subsequently, it could be seen from curve *c* of Figure 3A that the ECL signal of the SnO_2 QDs/MnO_2 NFs/GCE in $S_2O_8^{2-}$ solution rose to 9698 a.u., which was approximately 1.8 times stronger than that of the SnO_2 QDs/GCE in $S_2O_8^{2-}$ solution (curve *b* in Figure 3A). Moreover, the reduction peak of the corresponding CV curve presented a more positive potential at -1.24 V (curve *c* in Figure 3B) compared with that of curve *b* in Figure 3B. The above phenomenon implied that the MnO_2 NFs not only acted as a co-reaction accelerator to promote the reduction of $S_2O_8^{2-}$, but also provided an effective matrix to capture a huge amount of SnO_2 QDs, thus enhancing the ECL intensity. After the Ag NPs were further introduced, the ECL signal of the Ag NPs/SnO_2 QDs/MnO_2 NFs/GCE in $S_2O_8^{2-}$ solution further rose to a maximum value of 12106 a.u. (curve *d* in Figure 3A). Similarly, the reduction peak potential of the corresponding CV curve was positively shifted to -0.92 V (curve *d* in Figure 3B). It suggested that as the second co-reaction accelerator, Ag NPs increased abundant catalytic active sites to further promote the reduction of $S_2O_8^{2-}$, which was consistent with the previously reported literature (Tu et al., 2020). With the introduction of dual co-reaction accelerators, the ECL signal of SnO_2 QDs (curve *d* in Figure 3A) was obviously 226% up compared with that of the single SnO_2 QDs in $S_2O_8^{2-}$ without any co-reaction accelerator (curve *b* in Figure 3A). The enhancement was ascribed to the strong synergistic effect, which not only supplied more available catalytic active sites, but also improved the electrochemical

reaction efficiency to output more strongly oxidizing intermediates ($SO_4^{\bullet-}$) by facilitating the reduction of $S_2O_8^{2-}$.

Then, to further figure out that MnO_2 NFs and Ag NPs could interact with $S_2O_8^{2-}$ to produce large amounts of $SO_4^{\bullet-}$, we analyzed ECL and CV profiles of three different modified electrodes in $S_2O_8^{2-}$ solution. When the MnO_2 NFs/GCE was measured in $S_2O_8^{2-}$ solution, the results showed that its ECL signal increased by 2.4 times (curve *f* in Figure 3A) compared to that of bare GCE in $S_2O_8^{2-}$ solution (curve *e* in Figure 3A). In addition, the reduction peak potentials of CV curve exhibited a positive shift from -1.38 V (curve *e* in Figure 3C) to -1.16 V (curve *f* in Figure 3C), and the peak current increased. A similar phenomenon occurred when the Ag NPs/GCE was measured in $S_2O_8^{2-}$ solution. These results further proofed that the MnO_2 NFs and Ag NPs could interact with $S_2O_8^{2-}$ to accelerate the reduction of $S_2O_8^{2-}$ for the significant increasement of $SO_4^{\bullet-}$.

3.4. Feasibility investigation of the biosensor

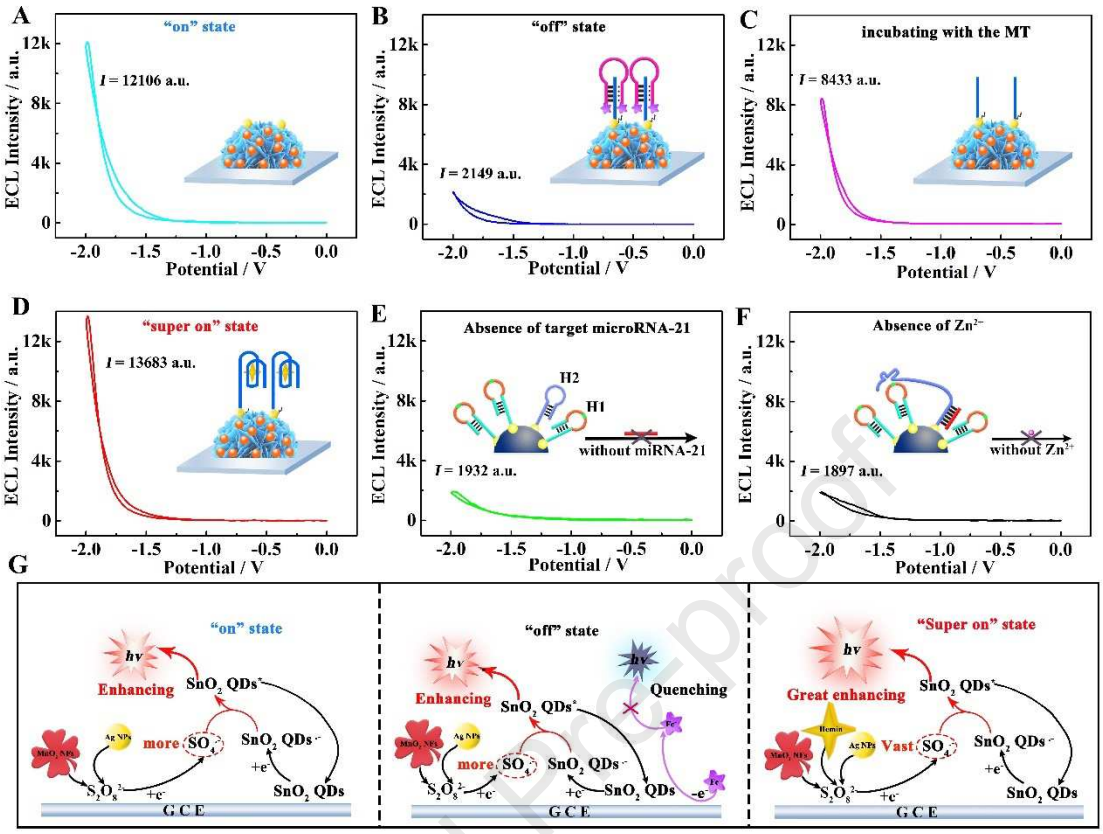

Fig. 4. ECL profiles of the designed ECL biosensor at different steps: (A) Ag NPs/SnO_2 QDs/MnO_2 NFs/GCE ("on" state), (B) Fc-DNA-Fc/HT/CP/Ag NPs/SnO_2 QDs/MnO_2 NFs/GCE ("off" state), (C) MT/Fc-DNA-Fc/HT/CP/Ag NPs/SnO_2 QDs/MnO_2 NFs/GCE, (D) Hemin/MT/Fc-DNA-Fc/HT/CP/Ag NPs/SnO_2 QDs/MnO_2 NFs/GCE ("super on" state), and of two control experiments: (E) without target miRNA-21 and (F) without Zn^{2+}. The test buffer: 2 mL PBS solution (pH = 7.4) containing 10 mM $S_2O_8^{2-}$. (G) Schematic illustration of possible ECL mechanism: "on" state, "off" state and "super on" state.

In order to verify the feasibility of this proposed biosensor for miRNA-21 detection based on 3D DNA walker amplification, the ECL signals of different steps were employed. As shown in Figure 4A, when the Ag NPs/SnO_2 QDs/MnO_2 NFs was modified on the GCE, an intensive ECL signal of 12106 a.u. was obtained as "on" state attributed to the synergistic effect between the high-efficiency dual co-reaction accelerators. After incubating with CP, HT, Fc-DNA-Fc successively, the triplex DNA structures were formed, and the ECL signal distinctly dropped down to 2149 a.u.

(Figure 4B) which achieved the "off" state owning to the quenching effect of ferrocene. Remarkably, after incubating with MT solution, the ECL signal recovered roughly 4 times as much as that of the "off" state (Figure 4C). This indicated that miRNA-21 could convert to MT, which enabled the Fc-DNA-Fc to remove from the electrode surface, thus realizing the signal recovery. When hemin was dropped onto the electrode surface, the CPs with G-rich sequence captured large quantities of hemin to form a great many hemin/G-quadruplex structures. And its ECL intensity was heightened significantly to the maximum of 13683 a.u (Figure 4D), where hemin/G-quadruplex acted as the third co-reaction accelerator, thus an extremely amplified ECL signal ("super on" state) was realized. Furthermore, the possible ECL mechanisms of "on" state, "off" state and "super on" state were illustrated in Figure 4G.

To investigate the feasibility of the target conversion process, the ECL responses of two control experiments without target miRNA-21 (Figure 4E) or without Zn^{2+} (Figure 4F) were measured. The ECL intensities were 1932 a.u. (Figure 4E) and 1897 a.u. (Figure 4F) respectively, which almost unchanged compared with that of the "off" state (Figure 4B). This pointed out that target miRNA-21 and Zn^{2+} were both essential components to successfully implement the 3D DNA walker amplification strategy.

3.5. Performance of the ECL biosensor toward miRNA-21 detection

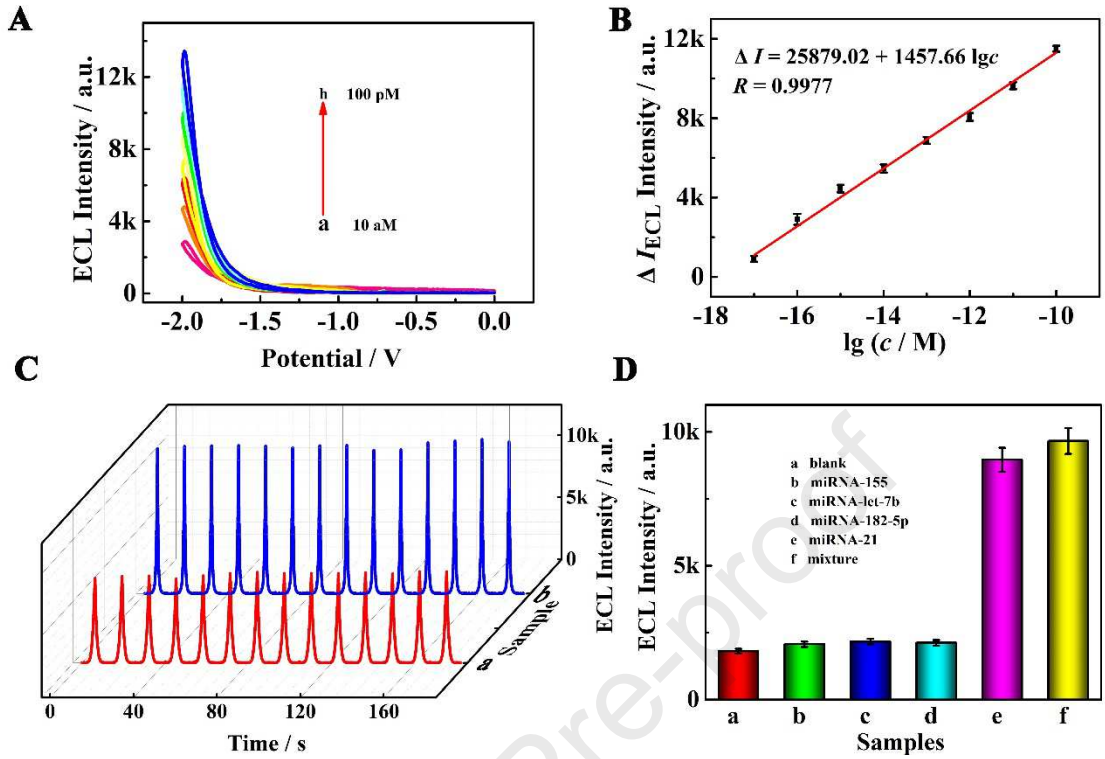

Fig. 5. (A) ECL response of the fabricated biosensor at varied miRNA-21 concentrations. (B) Calibration curve for the ΔI_{ECL} versus the logarithm of miRNA-21 concentration. (C) Stability of the ECL biosensor at 10 fM (red line) and 10 pM (blue line) miRNA-21. (D) Selectivity of this sensing platform for different targets: (a) blank, (b) miRNA-155 (10 pM), (c) miRNA-let-7b (10 pM), (d) miRNA-182-5p (10 pM), (e) miRNA-21 (100 fM) and (f) mixture including 100 fM miRNA-21, 10 pM miRNA-155, 10 pM miRNA-let-7b, 10 pM miRNA-182-5p. Error bars, SD, n = 3.

Based on the optimal experimental conditions, the analytical performance of this proposed biosensor toward miRNA-21 was investigated. As shown in Figure 5A, the ECL response signal enhanced gradually following the growth of miRNA-21 concentrations (10 aM to 100 pM). From the corresponding calibration curve in Figure 5B, it was apparent to find that an outstanding linear relationship existed between the ΔECL intensities (ΔI_{ECL}) and the logarithm of miRNA-21 concentrations (lg *c*). The regression equation was fitted as ΔI = 25879.02 + 1457.66 lg *c*, and a correlation coefficient (R) was 0.9977. At a signal-to-noise ratio (S/N) of 3, the detection limit of 2.9 aM for the proposed biosensor could be estimated (the

calculation procedure is shown in Section 10 of the Supporting Information). In addition, the comparison results between this designed ECL biosensor and other analytical methods were exhibited in Table S2, testifying that the designed biosensor possessed a superior detection sensitivity for miRNA.

Subsequently, we assessed two other important performance parameters of the proposed biosensor including stability and selectivity. The stability was evaluated by analyzing the fluctuation of ECL intensity under 14 cycles of continuous CV scanning. According to Figure 5C, the ECL intensity could remain a stable response at each different miRNA-21 concentration of 10 fM and 10 pM, and the relative standard deviation (RSD) was 2.59% (red line) and 2.15% (blue line) respectively, which proved that this constructed biosensor possessed excellent stability toward miRNA-21 detection. To further explore the selectivity toward miRNA-21, the proposed biosensor was measured with target miRNA-21 and three interference miRNAs including miRNA-155, miRNA-let-7b and miRNA-182-5p. The concentrations of the interference substances (10 pM) were set to 10 times higher than that of the target miRNA-21 (100 fM). As displayed in Figure 5D, the ECL intensity of three interference miRNAs was negligibly different from that of the blank. Moreover, the target miRNA-21 exhibited similar intensity compared with the mixture solution. These results fully proved the prominent stability and selectivity of the proposed biosensor toward miRNA-21 detection.

3.6. Application of the biosensor in cancer cells

To investigate the capability of this proposed biosensor in real samples, the lysates of human breast cancer cells (MCF-7) and cervical cancer cells (Hela) were

chosen to accomplish the ECL analysis. As shown in Figure 6, with the growth of MCF-7 cell concentration (from 10^1 to 10^6 cells), the corresponding ECL response increased significantly, indicating that miRNA-21 was extremely expressed in MCF-7 cells. However, the Hela cells showed much lower ECL response compared to MCF-7 cells under the same experimental conditions. It was clear from the above comparison results that miRNA-21 exhibited higher expression in MCF-7 cells than that in Hela cells, which conformed to the reported literature values (Xu et al., 2020). In consequence, the proposed biosensor had great potential for miRNA-21 detection in clinical diagnosis.

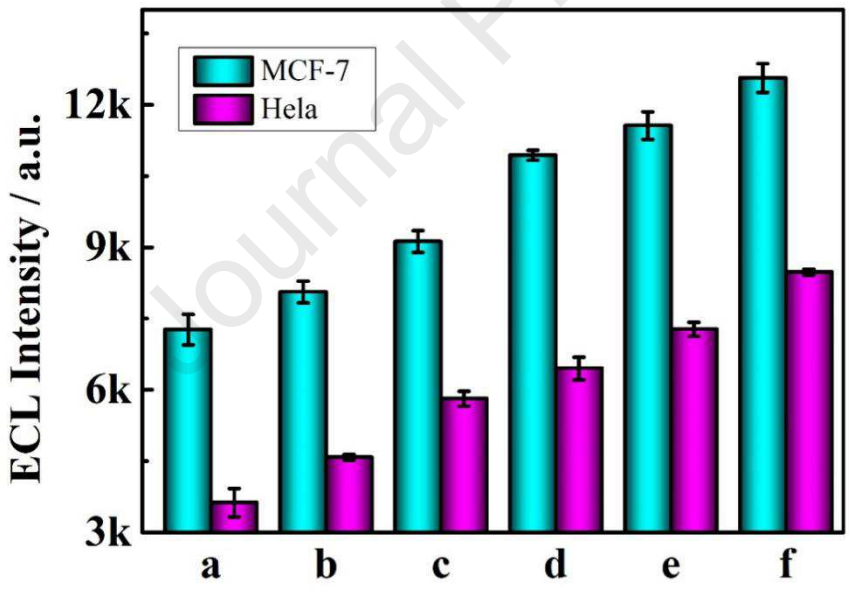

Fig. 6. ECL response of this proposed biosensor in MCF-7 and Hela cells: (a) 10, (b) 10^2, (c) 10^3, (d) 10^4, (e) 10^5 and (f) 10^6 cells.

4. Conclusion

In summary, a remarkably strong ECL emission of SnO_2 QDs was achieved by the synergistic promotion strategy based on three types of co-reaction accelerators for the first time where the MnO_2 NFs, Ag NPs and hemin/G-quadruplex were acted as

co-reaction accelerators. Benefiting from the synergistic effect, the deft integration of three types of co-reaction accelerators had many merits such as better structural stability, more exposed catalytic active sites, and faster charge transfer, which led to an extraordinary enhancement in ECL intensity. Furthermore, this novel "on-off-super on" ECL biosensor was developed to implement the ultrasensitive detection of miRNA-21 based on the synergistic promotion strategy and 3D DNA walker machine. Importantly, this work not only shed a new insight into the fabrication of high-performance co-reaction accelerators by the rational material selection and rigorous structural design, but also highlighted a powerful avenue for highly-sensitive and specific detection of microRNA in biochemical analysis and clinical diagnosis.

Acknowledgments

This work was financially supported by the NNSF of China (22022408 and 21675130), the Chongqing Talents Personnel Support Program (CQYC201905067), the Fundamental Research Funds for the Central Universities (XDJK2019TJ002) and phD research startup foundation of Panzhihua University (BKQJ2019047).

Appendix A. Supplementary data

Supplementary data to this article can be found online at

References

Bruchez, M., Moronne, M., Gin, P., Weiss, S., Alivisatos, A.P., 1998. Science 281, 2013-2016.

Chu, K., Liu, Y.P., Li, Y.B., Wang, J., Zhang, H., 2019. ACS Appl. Mater. Interfaces 11, 31806-31815.

Chen, S., Zhu, J.W., Wu, X.D., Han, Q.F, Wang, X., 2010. ACS Nano 4, 2822-2830.

Dai, W.X., Zhang, L., Zhao, W.W., Yu, X.D., Xu, J.J., Chen, H.Y., 2017. Anal. Chem. 89, 8070-8078.

Dutta, D., Chandra, S., Swain, A.K., Bahadur, D., 2014. Anal. Chem. 86, 5914-5921.

Ding, Z.F., Quinn, B.M., Haram, S.K., Pell, L.E., Korgel, B.A., Bard, A.J., 2002. Science 296, 1293-1297.

Dong, Y.P., Wang, J., Peng, Y., Zhu, J.J., 2017. Biosens. Bioelectron. 94, 530-535.

Fabrizio, E.F., Prieto, I., Bard, A.J. 2000. J. Am. Chem. Soc. 122, 4996-4997.

Gao, L., Wu, G.S., Ma, J., Jiang, T.C., Chang, B., Huang, Y.S., Han, S., 2020. ACS Appl. Mater. Interfaces 12, 12982-12989.

Keyikoglu, R., Karatas, O., Khataee, A., Kobya, M., Can, O.T., Soltani, R.D.C.S., Isleyen, M., 2020. Sep. Purif. Technol. 247, 1383-5866.

Kitamura, Y., Mishio, K., Arslan, P., Ikeda, B., Imoto, C., Katsuda, Y., Ihara, T., 2020. Anal. Sci. 36, 959-964.

Khan, A.U., Kasha, M., 1970. J. Am. Chem. Soc. 92, 3293-3300.

Khan, M.S., Ameer, H., Ali, A., Li, Y.Y., Yang, L., Ren, X., Wei, Q., 2020. Biosens. Bioelectron. 162, 112235-112242.

Lu, S.Q., Yan, D.L., Chen, L., Zhu, G.S., Xu, H.R., Yu, A.B., 2016. Mater. Lett. 168, 40-43.

Li, H.Y., Lin, H.Y., Lv, W.X., Gai, P.P., Li, F., 2020. Biosens. Bioelectron. 165, 112336-112343.

Li, W., Rong, Y.C., Wang, J.Y., Li, T.Z., Wang, Z.G., 2020. Biosens. Bioelectron. 169, 112605-112612.

Lei, Y.M., Zhuo, Y., Guo, M.L., Chai, Y.Q., Yuan, R., 2020. Anal. Chem. 92, 2839-2846.

Ma, M.N., Zhuo, Y., Yuan, R., Chai, Y.Q., 2015. Anal. Chem. 87, 11389-11397.

Myung, N., Ding, Z.F., Bard, A.J., 2002. Nano Lett. 2, 1315-1319.

Reddy, A.L.M., Shaijumon, M.M., Gowda, S.R., Ajayan, P.M., 2009. Nano Lett. 9, 1002-1006.

Shi, R., Cao, Y.H., Bao, Y.J., Zhao, Y.F., Waterhouse, G., Fang, Z.Y., Wu, L.Z., Tung, C.H., Yin, Y.D., Zhang, T.R., 2017. Adv. Mater. 29, 1700803-1700809.

Shifrina, Z.B., Matveeva, V.G., Bronstein, L.M., 2020. Chem. Rev. 120, 1350-1396.

Tu, T.T., Lei, Y.M., Chai, Y.Q., Zhuo, Y., Yuan, R., 2020. ACS Appl. Mater. Interfaces 12, 3945-3952.

Wang, Y.G., Fan, D.W., Zhao, G.H., Feng, J.H., Wei, D., Zhang, N., Cao, W., Du, B., Wei, Q., 2018. Biosens. Bioelectron. 120, 1-7.

Wang, S.S., Ellington, A.D., 2019. Chem. Rev. 119, 6370-6383.

Xu, X.X., Zhuang, J., Wang, X., 2008. J. Am. Chem. Soc. 130, 12527-12535.

Xue, S.Y., Jing, P., Xu, W.J., 2016. Biosens. Bioelectron. 86, 958-965.

Xu, H.H., Jiang, L.P., Wang, J., Gao, Y.H., Luo, X.L., 2020. ACS Appl. Mater. Interfaces 12, 373-379.
Yang, X., Yu, Y.O., Peng, L.Z., Lei, Y.M., Chai, Y.Q., Yuan, R., Zhuo, Y., 2018. Anal. Chem. 90, 3995-4002.
Zhang, Y.F., Wang, M., Wang, Y.G., Feng, J.H., Zhang, Y., Sun, X., Du, B., Wei, Q., 2019. Biosens. Bioelectron. 126, 23-29.
Zhu, S.S., Jin, C., Duan, X.G., Wang, S.B., Ho, S.H., 2020. Chem. Eng. J. 393, 1385-8947.
Zheng, L.Y., Chi, Y.W., Dong, Y.Q., Lin, J.P., Wang, B.B., 2009. J. Am. Chem. Soc. 131, 4564-4565.
Zhou, J.J., Li, Y., Wang, W.J., Tan, X.C., Lu, Z.C., Han, H.Y., 2020. Biosens. Bioelectron. 164, 112332-112344.
Zhou, X.M., Zhang, W., Wang, Z., Han, J., Xie, G., Chen, S.P., 2020. Biosens. Bioelectron. 148, 111795-111802.

Highlights

1. A synergistic promotion strategy was used to achieve an efficient SnO_2 QDs-based ternary ECL system.
2. An extraordinarily strong ECL signal of SnO_2 QDs was obtained based on the synergistic effect of three types of co-reaction accelerators.
3. The “on-off-super on” ECL biosensor was successfully constructed for the ultrasensitive detection of miRNA-21.

Declaration of interests

☒ The authors declare that they have no known competing financial interests or personal relationships that could have appeared to influence the work reported in this paper.

☐The authors declare the following financial interests/personal relationships which may be considered as potential competing interests: